Effect of Gap Junction Distribution, Size, and Shape on the Conduction Velocity in a Cell-by-Cell Model for Electrophysiology

Giacomo Rosilho de Souza[1][0000−0002−0176−8455], Simone Pezzuto[1,2][0000−0002−7432−0424], and Rolf Krause[1][0000−0001−5408−5271]

[1] Center for Computational Medicine in Cardiology, Euler Institute, Università della Svizzera italiana, Lugano, Switzerland
{giacomo.rosilhodesouza,rolf.krause}@usi.ch
[2] Department of Mathematics, Università di Trento, Povo, Italy
simone.pezzuto@unitn.it

Abstract. Gap junction arrangement is a major determinant of cardiac conduction velocity. Importantly, structural remodeling of the myocardium may lead to pathological CV and a pro-arrhythmic substrate. In this work we aim at quantifying the side-to-side conduction velocity in a sub-micrometer model of the myocardium that accounts for gap junctions. We consider the Extracellular-Membrane-Intracellular (EMI) model, which describes the evolution of the electric potential within each cell and in the extracellular space. For the solution of the model, we propose a boundary integral formulation of the cell-to-cell model that leads to small system of ODEs. We study several configurations of lateral gap junction distribution, as well as different shapes and sizes of the cell-to-cell connection. We find that irregular positioning of gap junctions from cell to cell is of utmost importance to obtain realistic CV values, while gap junction's shape is of secondary importance.

Keywords: Electrophysiology · Cell-by-Cell Model · Gap Junctions · EMI Model · Boundary Element Method.

1 Introduction

The cardiac tissue has a complex cellular and subcellular organization. Most of the myocardium is occupied by cardiomyocytes, excitable cells responsible for electric propagation and active force generation. Cardiomyocytes form the cardiac syncytium, a network of tightly connected cells that ensures a smooth propagation of the action potential [8]. Macroscopically, the propagation appears anisotropic because cell-to-cell coupling occurs mostly in the longitudinal direction, yielding a fiber bundle structure. Transverse-to-fiber conduction is generally much slower, of a ratio 1:3 to 1:6 [12]. Several factors compete for the anisotropy ratio. Gap junctions distribution is of utmost importance. Gap junctions are responsible for the cell-to-cell coupling, and are mostly found in the fiber direction, with only a few of them in the lateral direction. Additionally,

transverse conduction is affected by geometrical factors such as cell thickness and branching.

In this work, we are interested in studying in a quantitative manner how lateral gap junction distribution and the geometry of the connection affect the macroscopic conduction velocity in the myocardium. For this, we consider an Extracellular-Intracellular-Membrane (EMI) model [18]. The EMI model is a degenerate parabolic PDE: stationary on the intra- and extra-cellular, but time-dependent on the transmembrane boundary. The EMI model is also coupled with a cellular membrane model. Within the EMI framework, the anisotropic propagation of the action potential results from the geometrical arrangement of the cells and the gap junction distribution. In contrast, the anisotropy ratio and electric conductivity in the standard bidomain model must be given *a priori*, e.g., based on experimental data. As a matter of fact, it has been shown that the bidomain model can be rigorously justified by a homogenization procedure applied the EMI model [9]. In particular, the intra- and extra-cellular conductivity tensors in the bidomain model could be estimated by solving a cell problem [11].

From a computational point of view, the EMI model is significantly more expensive than the bidomain model [10], and it requires fine meshes [18]. Since we are interested only in the transmembrane potential, we adopt here a boundary integral formulation of the problem that avoids the computation of the intra- and extra-cellular potentials. In this way, we recast the full EMI model to a set of ordinary differential equations with a structure similar to the monodomain equation [15]. The reduced membrane model, fully equivalent to the original EMI formulation, only lives on the membrane domain. Thus, we can employ an unprecedented spatial resolution (below 1 µm) for simulating gap junctions. Finally, thanks to a fast boundary element implementation, we can quickly explore multiple realizations of gap junctions distribution, thus assessing the conduction velocity in a statistical manner.

2 Methods

The EMI model considers cells represented by bounded domains $\Omega_i \subset \mathbb{R}^d$, $d \geq 2$, for $i = 1, \ldots, N$, all embedded in a extracellular space denoted by $\Omega_0 \subset \mathbb{R}^d \setminus \cup_{i=1}^N \bar{\Omega}_i$. The electric potential is in general discontinuous, with jumps across cell-to-cell boundaries and the cellular membrane. We denote by u_i, $i = 0, \ldots, N$, the electric potential in the subdomain Ω_i. We denote the interfaces with $\Gamma_{ij} = \Gamma_i \cap \Gamma_j$, $0 \leq i, j \leq N$, where $\Gamma_i = \partial\Omega_i$. The intercellular connections, named gap junctions, occur at Γ_{ij} for $1 \leq i, j \leq N$, whereas the transmembrane boundaries are Γ_{i0}. The outer boundary is $\Sigma = \partial\Omega_0 \setminus \bigcup_{i=1}^N \Gamma_{i0}$. The normals $\boldsymbol{n}_i$ point

outwards to Ω_i. The EMI model reads as follows:

$$\begin{cases} -\sigma_i \Delta u_i = 0, & \text{in } \Omega_i \text{ for } i = 0, \dots, N, \quad (1a) \\ -\sigma_i \partial_{\boldsymbol{n}_i} u_i = C_{\mathrm{m}} \partial_t V_i + I_{\mathrm{ion}}(V_i, z_i), & \text{on } \Gamma_{i0} \text{ for } 1 \le i \le N, \quad (1b) \\ -\sigma_0 \partial_{\boldsymbol{n}_0} u_0 = \sigma_i \partial_{\boldsymbol{n}_i} u_i, & \text{on } \Gamma_{i0} \text{ for } 1 \le i \le N, \quad (1c) \\ u_i - u_0 = V_i, & \text{on } \Gamma_{i0} \text{ for } 1 \le i \le N, \quad (1d) \\ \partial_t z_i = g(V_i, z_i), & \text{on } \Gamma_{i0} \text{ for } 1 \le i \le N, \quad (1e) \\ -\sigma_i \partial_{\boldsymbol{n}_i} u_i = \kappa(u_i - u_j) & \text{on } \Gamma_{ij} \text{ for } 1 \le i, j \le N, \quad (1f) \\ -\sigma_0 \partial_{\boldsymbol{n}_0} u_0 = 0, & \text{on } \Sigma. \quad (1g) \end{cases}$$

The electric conductivities, denoted by σ_i, $i = 0, \dots, N$, are assumed constant but possibly different from each other. The membrane electric capacitance is C_{m}, I_{ion} represents the sum of ionic currents and z_i are vectors representing the ionic model's state variable. We note that the system is stationary on the cellular and extracellular domains, as well as on the gap junctions where an algebraic condition is imposed (with permeability κ). Time dynamics occur only on the transmembrane boundary $\Gamma_m = \cup_{i=1}^{N} \Gamma_{i0}$.

Problem (1) has already been solved by means of the finite element method [17,18]. With the boundary element method (BEM), it has been solved only for simple geometries of isolated cells [4,6,7]. Here, we consider the BEM approach proposed in [15], with no geometrical restriction on the problem. For the numerical solution of Eq. (1) we make use of the following result (see [15] for a proof.)

Theorem 1. *The BEM space discretization of* (1) *is equivalent to the ordinary differential equations system*

$$\begin{cases} C_m \dfrac{\mathrm{d}\boldsymbol{V}_m}{\mathrm{d}t} + I_{ion}(\boldsymbol{V}_m, \boldsymbol{z}) = \psi(\boldsymbol{V}_m), & (2a) \\ \dfrac{\mathrm{d}\boldsymbol{z}}{\mathrm{d}t} = g(\boldsymbol{V}_m, \boldsymbol{z}), & (2b) \end{cases}$$

where $\psi(\boldsymbol{V}_m) = \boldsymbol{\lambda}_m$ *and* $\boldsymbol{\lambda}_m \in \mathbb{R}^{M_m}$, $\boldsymbol{\lambda}_g \in \mathbb{R}^{M_g}$, $\boldsymbol{\beta} \in \mathbb{R}^N$ *are solutions to*

$$\begin{pmatrix} F_{mm} & F_{mg} & A_m G \\ F_{gm} & F_{gg} - \kappa^{-1} I & A_g G \\ G^\top A_m^\top & G^\top A_g^\top & 0 \end{pmatrix} \begin{pmatrix} \boldsymbol{\lambda}_m \\ \boldsymbol{\lambda}_g \\ \boldsymbol{\beta} \end{pmatrix} = \begin{pmatrix} \boldsymbol{V}_m \\ \mathbf{0} \\ \mathbf{0} \end{pmatrix}, \quad (3)$$

with

$$F_{mm} = A_m F A_m^\top, \quad F_{mg} = A_m F A_g^\top, \quad F_{gm} = A_g F A_m^\top, \quad F_{gg} = A_g F A_g^\top. \quad (4)$$

For the space discretization of (1) we adopt a collocation BEM with trigonometric Lagrange basis functions and, in Theorem 1, M_m and M_g represent the number of collocation nodes lying on the transmembrane boundary Γ_m and on

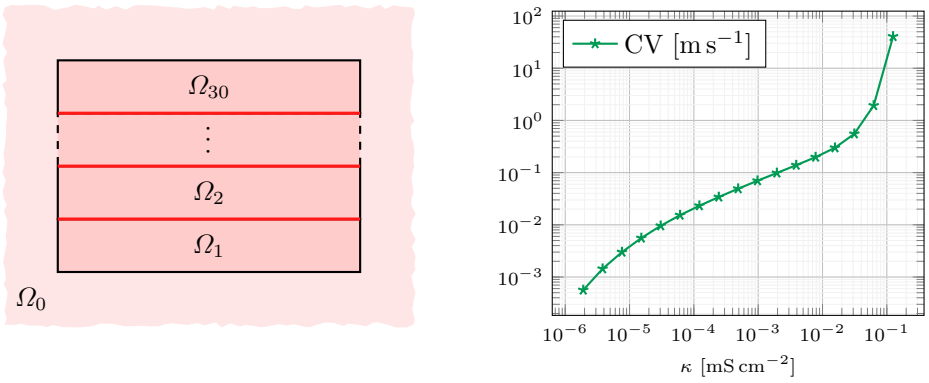

Fig. 1. Conduction velocity across a vertical array of 30 cells. Red boundaries represent gap junctions with uniform permeability κ. Each cell is 100 µm long and 10 µm thick. On the right, the CV for increasing values of κ.

the union of all gap junctions $\Gamma_g = \cup_{i,j=1,i\neq j}^{N} \Gamma_{ij}$. Variables $\boldsymbol{V}_\mathrm{m}$ and $\boldsymbol{z}$ are the spatial discretizations of V_i and z_i, $i = 1, \ldots, N$, respectively. Therefore, ODE (2) lives on the transmembrane boundary Γ_m and the remaining model constraints, as Laplace problems, flux continuities and gap junction algebraic conditions, are encoded into the linear map ψ defined by the linear system (3).

Every time that $\psi(\boldsymbol{V}_\mathrm{m})$ has to be evaluated, e.g. when approximating (2) with a time marching scheme, system (3) has to be solved. This system is symmetric and has size $M_m + M_g + N$ hence, when the number of degrees of freedom is not overly large, it is factorized only once. This is the approach adopted here.

Let $M = M_m + M_g$, matrices $A_m \in \mathbb{R}^{M_m \times M}$, $A_g \in \mathbb{R}^{M_g \times M}$ are projection operators, from a global system of degrees of freedom representing functions on $\Gamma_m \cup \Gamma_g$ to local ones. Matrix $F \in \mathbb{R}^{M \times M}$ encodes Laplace equations in all subdomains Ω_i, $i = 0, \ldots, N$, and flux continuities. It is based on pseudo inverses of the Dirichlet-to-Neumann maps. Matrix $G \in \mathbb{R}^{M \times N}$ enforces condition $V_i = u_i - u_0$ and as well solvability of problems involving pseudo inverses.

Finally, for the time integration of (2) we employ the mRKC method [1], which is a multirate explicit stabilized method.

3 Numerical Results

In this section we report four numerical experiments. The main goal is to investigate dependence of conduction velocities (CVs) on the distribution, size and shape of the gap junctions on the cellular boundaries parallel to the fiber direction. In all experiments, parameters are set as following [17]: $C_\mathrm{m} = 1\,\mu\mathrm{F\,cm^{-2}}$, $\sigma_e = 20\,\mathrm{mS\,cm^{-1}}$, $\sigma_i = 3\,\mathrm{mS\,cm^{-1}}$, and $\kappa = 1/R_m = 690\,\mathrm{mS\,cm^{-2}}$. For the membrane, we consider the Courtemanche-Ramirez-Nattel model [3].

In the first experiment, we evaluate the transverse CV in a vertical array of 30 cells, as shown in Figure 1 (left panel). For the experiment, we considered

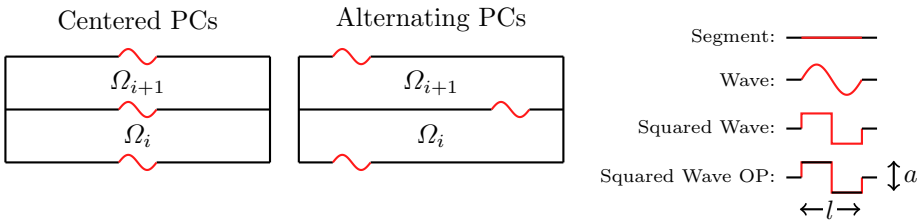

Fig. 2. Cells with non-zero permeability κ only on the Permeable Curve (PC), indicated in red. We consider aligned and centered PCs (left panel), and alternating PCs (middle panel). PC are also parametrized with different shapes (right panel), amplitude a, and length l.

the parameters given as above, except for the gap junction permeability κ. The transverse CV is defined as the difference in activation time between last and first cell boundary in the array, over their distance (300 µm). The activation time at x is set as the earliest time of $V_{\mathrm{m}}(x,t) > -60\,\mathrm{mV}$. As shown in the right panel of Figure 1, when we vary the permeability κ the transverse CV increases rapidly. In particular, the value of $\kappa = 690\,\mathrm{mS\,cm^{-2}}$ yields a very high, non-physiological value of velocity by several orders of magnitude. In fact, a physiological value of CV, e.g., $0.1\,\mathrm{m\,s^{-1}}$ to $0.2\,\mathrm{m\,s^{-1}}$ would be achieved by a value of κ of the order of $10^{-2}\,\mathrm{mS\,cm^{-2}}$. We conclude that only a very small portion of the boundary should be permeable.

Hence, in the second experiment we consider a similar setup of 30 vertically-stacked cells, but now the permeable portion of the boundary is small, between 1% and 15% of the whole length. We also vary the shape of the connection, from flat to wave-like, and its position along the boundary. Henceforth, we call "Permeable Curve" (PC) the permeable portion of the boundary. In Figure 2 we report different options for the PC. The connection is parameterized with the length l and the amplitude a of the PC.

The results of the second experiment are summarized in Figure 3. Firstly, we notice that there is a major difference in CV when moving from an aligned pattern of PCs (first row of Figure 3) to an alternating pattern (second row). In the case of aligned PCs, the CV is always above $1\,\mathrm{m\,s^{-1}}$, thus non-physiological, for all combinations of PC shape and size. We also tested the case of PCs are not centered but still aligned, and the results are the same (not shown). This suggests that gap junction alignment between cells can sensibly enhance the transverse CV. On the other hand, alternating PCs yields realistic values of CV for a wide range of shape parameters. A lack of alignment of gap junctions in the transverse direction is indeed possible, in contrast to the longitudinal direction. (However, in the fiber direction the cell is elongated, and we expect less end-to-end influence between gap junctions.)

It is also interesting to observe how CV varies with PC shape and size (see Figure 3). The flat configuration always yields the fastest conduction, as expected. For large l, the flat PC is very similar to the "Wave" PC in terms of

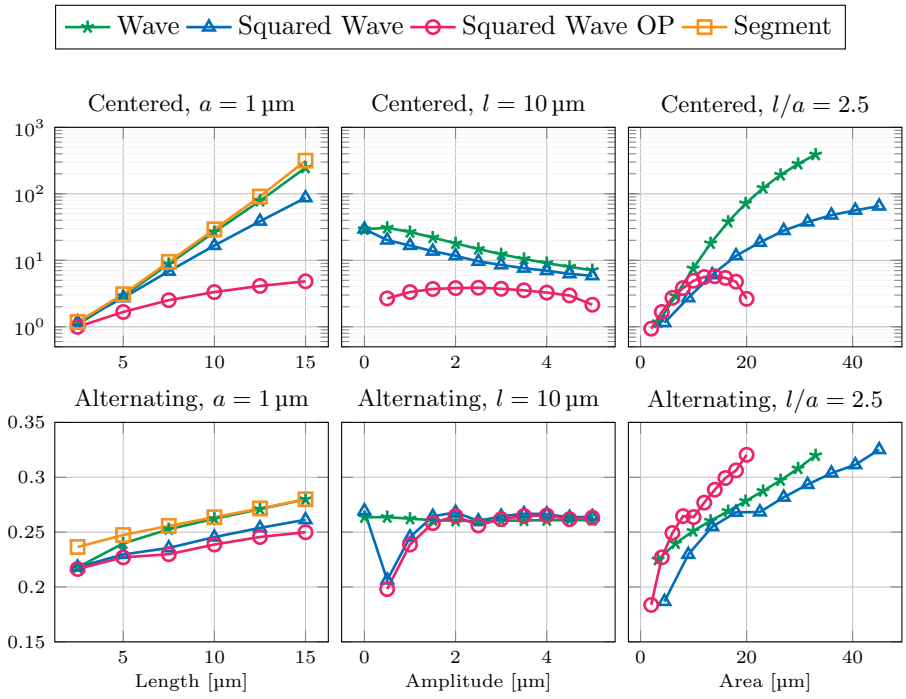

Fig. 3. Transversal CV $[\mathrm{m\,s^{-1}}]$ for different shapes and positions of the Permeable Curve (PC). For area we mean the surface area of the PC, which in $\mathbb{R}^2$ is the length. For Squared Wave, for instance, the area is $2a + l$, and for Squared Wave OP is $2a$. We vary the area by varying l and a, while keeping the ratio $l/a = 2.5$ constant.

CV, but this is not the case for the other shapes. Somewhat paradoxically, the "Wave" and "Squared Wave" shapes do not always lead to similar CVs, although the difference is small. We conjecture that the contact area along the propagation direction, rather than the total area is what matters in determining the CV. This is quite apparent in the "Squared Wave OP" case, where the CV is generally lower than the other cases. Interestingly, here we still observe an increase in CV with l, which is due to the permeable vertical segments being better distributed along the cell's side, allowing the potential to propagate more uniformly through it. We also report that increasing the amplitude a of the PC leads to a decrease in CV for the "Wave" and "Squared Wave" shape. This is due to a decrease in smoothness of the propagation, when the amplitude of the PC is too large compared to its length. In summary, the major determinant of transverse CV in this experiment is gap junction alignment, followed by the length and smoothness of the PC.

The third experiment aims at exploring more in detail the effect of alignment of gap junctions. In fact, within a block of cells, the location of gap junctions is likely not structured. In this experiment we consider again the same array of

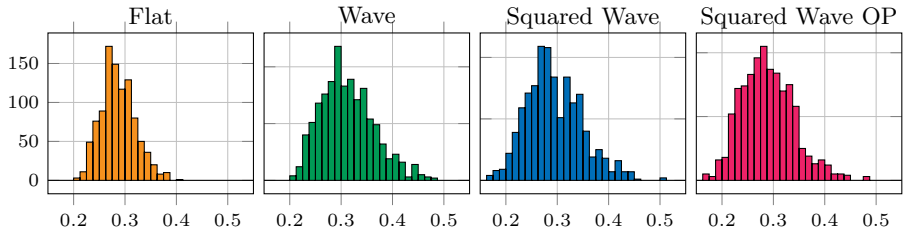

Fig. 4. Transverse CV distribution for randomly positioned PCs in a vertical array of 30 cells. For a graphical representation of PC shapes we refer to Figure 2.

cells, however the position of the PCs is randomized. For every shape of PC (see Figure 2) we perform 1000 experiments. For each experiment, the PC relative position p follows a uniform distribution $p \sim \mathcal{U}(l/c_l, 1 - l/c_l)$, where $c_l = 100\,\mu\text{m}$ is the cell length. The length l and amplitude a of the PC are respectively fixed to $2.5\,\mu\text{m}$ and $1\,\mu\text{m}$, except for the Segment PC where $l = 0.5\,\mu\text{m}$. With this choices, for all PC shapes we recover a CV of $0.2\,\text{m}\,\text{s}^{-1}$ when $p = 0.2$ with alternation, similarly to Figure 2, middle panel.

The resulting distribution of CV is displayed in Figure 4. Interestingly, CV values are physiological in all cases, and the dispersion is low. The average CV is approximately $0.3\,\text{m}\,\text{s}^{-1}$ in all cases. The standard deviation is lower in the case of flat PC ($0.033\,\text{m}\,\text{s}^{-1}$), when compared to the other PC shapes ($0.051\,\text{m}\,\text{s}^{-1}$). Since the PC are positioned randomly, an alignment is unlikely to occur and the potential propagates following a zigzag curve, similarly to the case of alternating PC positioning of the previous experiment. The smaller standard deviation of the "Segment" PC is hard to explain. The histograms in Figure 4 suggest that fast CVs are less likely to occur in the "Segment" case, thus reducing the dispersion.

The final experiment uses a 2-dimensional array of 20×20 cells, with a stimulus delivered at the bottom-left corner. In particular, we study how random deactivation of transversal PCs affect longitudinal, transversal and diagonal CVs. In a way, we are trying to mimic random deposition of endomysial fibrosis, as observed in the atria in patients with atrial fibrillation [13]. Here, we consider flat PCs with length $l = 0.5\,\mu\text{m}$. For fixed $P \in [0, 1]$, we run $M = 40$ experiments where transversal PCs are randomly placed and their conductivity κ is set to zero with probability P. Next, we compute the average longitudinal, transversal and diagonal CVs over the M experiments.

In Figure 5 we display the average CVs and confidence interval of one standard deviation with respect to the probability P. As expected, a decrease in transversal PCs permeability is associated with a decrease in diagonal and transversal CV. A block in conduction occurs for a large value of $P > 0.8$. The CV decreases also in the longitudinal direction as P increases, and it is about a half of its original value for $P = 1$. This is because the lower fiber of cells is isolated from the rest of the tissue, since the top boundary has zero current flux. Finally, the standard deviation is very small for the transversal CV,

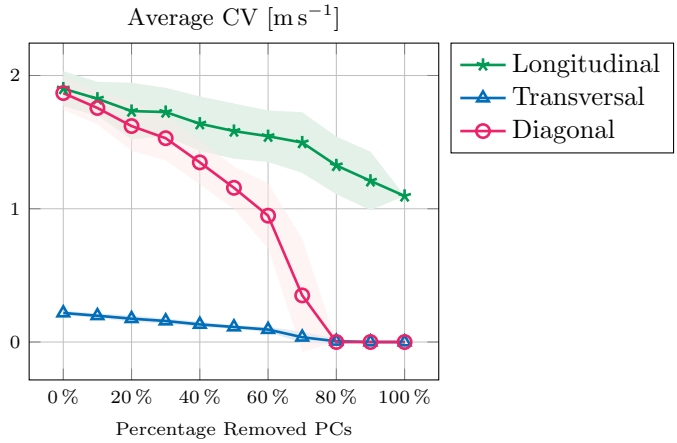

Fig. 5. Average longitudinal, transversal, and diagonal conduction velocities when transversal PCs are deactivated with probability P. The shaded area represents the confidence interval of one standard deviation.

because it is computed on the left boundary and so the signal does not cross the whole tissue. In contrast, the diagonal CV standard deviation is very high for the same reason.

4 Discussion

In this work we show that the transverse conduction velocity in a sub-µm microstructural model of cardiac tissue is strongly affected by lateral gap junction distribution and shape. We found that the major determinant of CV is the cell-to-cell alignment of gap junctions. The CV is non-physiologically fast when gap-junctions are vertically aligned. A lack of alignment leads to a transverse CV of $0.1\,\mathrm{m\,s^{-1}}$ to $0.3\,\mathrm{m\,s^{-1}}$, within a physiological range. The second determinant of CV is the smoothness of the cell-to-cell connection or permeable curve, but only the case of aligned gap junctions. These results are statistically robust, in the sense that also a random distribution of gap junctions yields similar CVs.

The EMI model can be effectively used to study the effect of gap junction remodeling in heart failure and cardiac arrhythmia [2]. It has been observed that gap junctions in a diseased myocardium may shift from a classical end-to-end (longitudinal) distribution towards a more side-to-side (transversal) arrangement, with a lower longitudinal CV [14]. In patients with history of atrial fibrillation, structural remodeling in terms of fibrosis is a major determinant of the arrhythmic substrate [13]. Here, endomysial fibrosis leads to endo-epicardial dissociation of the propagation due to a reduced transmural coupling of the myocardium [5]. This is consistent with the last numerical experiment, where transverse velocity is significantly reduced.

This work has some limitations too. We focused only on 1-D and 2-D cell arrangements, with cells of fixed shape and size. We also did not include the extracellular space between cells in all our experiments, since cell-to-cell distance is typically less than 0.2 µm, see Spach *et al.* [16]. In reality, the myocardium has a complex 3-D structure with branching and extracellular space surrounding most of the cells. Reproducing this arrangement in 2-D is difficult if not impossible. We are working on extending the BEM formulation of the EMI model to the 3-D case. We believe that our implementation of the EMI model is fast and sufficiently flexible for studying complex geometries. In conclusion, our model can be used to determine CVs to be employed in the a bidomain or monodomain formulation, e.g., in cases where the tissue presents fibrosis, and the effective model parameters are hard to determine experimentally.

Acknowledgments

This work was supported by the European High-Performance Computing Joint Undertaking EuroHPC under grant agreement No 955495 (MICROCARD) co-funded by the Horizon 2020 programme of the European Union (EU) and the Swiss State Secretariat for Education, Research and Innovation.

References

1. Abdulle, A., Grote, M.J., Rosilho de Souza, G.: Explicit stabilized multirate method for stiff differential equations. Mathematics of Computation **91**, 2681–2714 (2022)
2. Corrado, D., Link, M.S., Calkins, H.: Arrhythmogenic right ventricular cardiomyopathy. New England journal of medicine **376**(1), 61–72 (2017)
3. Courtemanche, M., Ramirez, R.J., Nattel, S.: Ionic mechanisms underlying human atrial action potential properties: insights from a mathematical model. American Journal of Physiology-Heart and Circulatory Physiology **275**(1), H301–H321 (1998)
4. Foster, K.R., Sowers, A.E.: Dielectrophoretic forces and potentials induced on pairs of cells in an electric field. Biophysical Journal **69**, 777–784 (1995)
5. Gharaviri, A., Bidar, E., Potse, M., Zeemering, S., Verheule, S., Pezzuto, S., Krause, R., Maessen, J.G., Auricchio, A., Schotten, U.: Epicardial fibrosis explains increased endo-epicardial dissociation and epicardial breakthroughs in human atrial fibrillation. Frontiers in Physiology **11**(68) (2020)
6. Henríquez, F., Jerez-Hanckes, C.: Multiple traces formulation and semi-implicit scheme for modelling biological cells under electrical stimulation. ESAIM: Mathematical Modelling and Numerical Analysis **52**, 659–702 (2018)
7. Leon, L.J., Roberge, F.A.: A model study of extracellular stimulation of cardiac cells. IEEE Transactions on Biomedical Engineering **40**, 1307–1319 (1993)
8. Neu, J., Krassowska, W.: Homogenization of syncytial tissues. Critical reviews in biomedical engineering **21**(2), 137–199 (1993)
9. Pennacchio, M., Savaré, G., Franzone, P.C.: Multiscale modeling for the bioelectric activity of the heart. SIAM Journal on Mathematical Analysis **37**(4), 1333–1370 (2005)

10. Pezzuto, S., Hake, J., Sundnes, J.: Space-discretization error analysis and stabilization schemes for conduction velocity in cardiac electrophysiology. International Journal for Numerical Methods in Biomedical Engineering **32**, e02762 (2016)
11. Richardson, G., Chapman, S.J.: Derivation of the bidomain equations for a beating heart with a general microstructure. SIAM Journal on Applied Mathematics **71**(3), 657–675 (2011)
12. Roth, B.J.: Electrical conductivity values used with the bidomain model of cardiac tissue. IEEE Transactions on Biomedical Engineering **44**(4), 326–328 (1997)
13. Schotten, U., Verheule, S., Kirchhof, P., Goette, A.: Pathophysiological mechanisms of atrial fibrillation: a translational appraisal. Physiological Reviews **91**(1), 265–325 (2011). https://doi.org/10.1152/physrev.00031.2009
14. Severs, N.J., Bruce, A.F., Dupont, E., Rothery, S.: Remodelling of gap junctions and connexin expression in diseased myocardium. Cardiovascular research **80**(1), 9–19 (2008)
15. de Souza, G.R., Krause, R., Pezzuto, S.: Boundary integral formulation of the cell-by-cell model of cardiac electrophysiology, submitted, arXiv:2302.05281
16. Spach, M.S., Heidlage, J.F.: The stochastic nature of cardiac propagation at a microscopic level: electrical description of myocardial architecture and its application to conduction. Circulation research **76**(3), 366–380 (1995)
17. Stinstra, J.G., Hopenfeld, B., MacLeod, R.S.: On the passive cardiac conductivity. Annals of Biomedical Engineering **33**, 1743–1751 (2005)
18. Tveito, A., Mardal, K.A., Rognes, M.E.: Modeling Excitable Tissue: The EMI Framework. Springer Nature (2021)